Development of 3D CFD model of compact steam methane reforming process for standalone applications

Ja-Ryoung Han*,**, Shinje Lee***,†, and Jong Min Lee*,†

*School of Chemical and Biological Engineering, Institute of Chemical Processes, Seoul National University,
1, Gwanak-ro, Gwanak-gu, Seoul 08826, Korea
**KOGAS Research Institute, Korea Gas Corporation, 1248, Suin-ro, Sangnok-gu, Ansan, Gyeonggi-do 15328, Korea
***Engineering Development Research Center, Seoul National University, 1, Gwanak-ro, Gwanak-gu, Seoul 08826, Korea

Abstract−The demand for sustainable energy has increased with growing concerns of environmental damage. H_2 has attracted considerable attention as a clean and renewable energy carrier that can be used in fuel cells. Industrial H_2 has been manufactured to produce synthetic gas in large-capacity plants using steam methane reforming (SMR). However, a compact H_2 production system is needed that maintains production efficiency on a small scale for fuel cell applications. In this study, a three-dimensional computational fluid dynamics model of a compact steam reforming reactor was developed based on the experimental data measured in a pilot-scale charging station. Using the developed model, one can predict all the compositions of the reformate produced in the reactor and simultaneously analyze the temperatures of the product, flue gas, and the reaction tube. Therewith, case studies were conducted to compare the H_2 production performance of the eight different structures and sizes of the proposed reformer. Based on the results, a design improvement strategy is proposed for an efficient small-scale SMR process.

Keywords: H_2 Fueling Station, Steam Methane Reforming, Compact Steam Reformer, Optimal Reactor Design, Reaction Kinetics, Computational Fluid Dynamics

INTRODUCTION

The demand for renewable energy utilizing H_2 is rapidly increasing to replace traditional carbon-based fossil fuel energy, owing to global environmental issues. Steam methane reforming (SMR) is the most promising, widely used, and well-developed technology to produce H_2, accounting for 95% of the H_2 produced in the U.S. [1]. SMR guarantees high thermal efficiency and cost-effectiveness per unit mole of hydrocarbon feedstock compared to other reforming methods, including partial oxidation reforming and auto thermal reforming. SMR is considered as a reasonable solution to supply H_2 not only for traditional large-scale industrial H_2 production systems but also for self-sustainable on-site H_2 fueling stations. Additionally, the residential and automotive consumption requirements are driving a strong demand for smaller and more portable SMR systems to meet the growing end-user need for H_2 fuel cell technologies [2]. Therefore, these demands for size flexibility lead to the need for creating more compact SMR reactors, while remaining highly efficient and dependable.

An H_2 production process typically comprises desulfurization, steam reforming, water-gas shift (WGS) reaction, and purification [3-6], and SMR accounts for the largest portion of the exergy or energy loss and destruction of the entire H_2 production process [5,6]. SMR runs the risk of maintaining dead volume in the furnace, which decreases thermal uniformity and efficient heat trans-

fer while increasing capital and maintenance costs. For decades, the improvement in thermal efficiency and productivity has been the most prevalent issue of industrial-scale SMR processes [7-9]. A variety of reactor design criteria for industrial-scale SMR reactors have been reported to solve the problem [10]. Numerous studies have been conducted on combustion, heat flux, and temperature distribution balancing of SMR reactors, because they directly affect the mechanical service life span and process efficiency of the reactor [11-15]. On the other hand, there is a lack of studies on optimized small-scale SMR reactors. It is because small-scale end-user SMR applications usually have a strictly limited installation area and a fixed production capacity, making the problem more difficult to solve.

Compact SMR systems can rely on computational fluid dynamics (CFD) to evaluate optimal reactor performance. CFD simulation has been widely used to understand detailed and complicated heat transfer and chemical reactions [16,17] and to determine geometric parameters for diverse types of reactors in many fields. Ansoni and Seleghim [21] used a CFD tool to optimize the injection angle and outlet-tube height of a continuous fermentation bioreactor by using a multi-objective evolutionary algorithm. Park et al. [22] present a CFD-based multi-objective optimal design of a chemical reactor with six design variables based on Bayesian optimization to reduce the number of iterations and computational costs [18-22].

For small-scale SMR reactors, Shin et al. [23] modified the heat recovery system of exhaust gas on a combustion engine for a stationary fuel cell SMR system and validated the temperature distribution by manipulating the feed gas composition and heat source flow rate, using a 3D CFD model validated with experimental

results [23]. They used the developed model to evaluate the methane conversion without considering the compositions of the other reactants. Hong et al. [24] validated the effect of catalyst-layer length and number of tubes of a 30 Nm³/h production scale SMR reactor with a detailed 3D numerical calculation, including the combustion chamber and its heat transfer, suggesting that increasing the number of reaction tubes from 6 to 8 would lead to improved system efficiency [24]. Nguyen et al. [25] suggested a 2.5 Nm³/h small-size sleeve-type SMR reactor and its optimal geometry by using a 3D CFD model with experimental data. They found an optimized gap size of the sleeve and flame shape according to burner type and its fuel compositions [25,26]. Although these 3D CFD models were demonstrated with experimental data on the reformate composition and the temperature profile of the catalyst layer, they did not consider the outlet temperature of the products and the combusted gases that are critical factors in designing downstream processes such as WGS reaction, purification, and heat recovery.

Despite the knowledge gained from previous studies, no 3D CFD model has been developed that can simultaneously predict the temperatures of the reaction tube, outlet, and all components of the reformate at various temperature distributions. There is room for further improvement because small-scale SMR reactors are typically installed at very precise locations and operated according to a fixed production capacity. These are the limitations associated with rigorous design requirements for achieving compact and efficient reactors. In this study, we propose a rigorous 3D CFD reactor model to overcome these limitations, validate the developed model using experimental data obtained from a commercial-scale real hydrogen refueling station, and investigate the design criteria for a small-size SMR reactor to minimize its size and maximize its productivity. The developed model is used to predict the composition of the product gas and the temperatures of the reaction tube, product gas, and flue gas. Eight distinct SMR reactor structures were considered to propose an optimal reactor configuration for a compact SMR system. By comparing the size and efficiency with a 30 Nm³/h SMR reactor installed at a pilot H₂/H₂ blended compressed natural gas (HCNG) fueling station as a reference model, we propose design improvement strategies and provide a suitable design standard for SMR reactors at real sites.

In Section 2, experimental procedures, including a reactor structure and operating conditions, are described. In Section 3, a 3D CFD model of SMR is developed and validated by comparing it with experimental data and theoretical equilibria. In Section 4, diverse reactor sizes and the productivity of the proposed SMR model are compared to identify an optimal compact configuration. Finally, Section 5 concludes the paper.
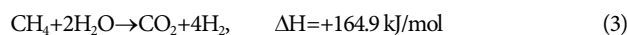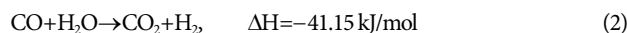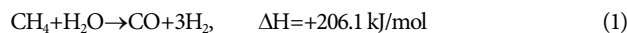
EXPERIMENTS

1. Reaction Kinetics of SMR

Steam reforming is a process to produce CO, CO_2, and H_2 from a hydrocarbon-based feedstock. It is advantageous under high-temperature and low-pressure conditions, owing to its strong endothermic reaction and Le Chatelier's principle, dependent on the stoichiometry of the overall reaction. It is divided into reforming reactions 1 and 3, and WGS reaction 2.

Table 1. Pre-exponential factors and activation energies for reaction kinetics [27]

A_1	A_2	A_3	E_1	E_2	E_3
4.225×10^{15}	1.955×10^{6}	1.020×10^{15}	240.1	67.13	243.9

$$CH_4 + H_2O \rightarrow CO + 3H_2, \quad \Delta H = +206.1 \, kJ/mol \tag{1}$$

$$CO + H_2O \rightarrow CO_2 + H_2, \quad \Delta H = -41.15 \, kJ/mol \tag{2}$$

$$CH_4 + 2H_2O \rightarrow CO_2 + 4H_2, \quad \Delta H = +164.9 \, kJ/mol \tag{3}$$

For reversible reactions, intrinsic SMR kinetics were derived from Xu and Froment [27], which are commonly used for CFD modeling of the SMR reactions applied in this study, as shown in Eqs. (4)-(7).

$$r_1 = \frac{k_1}{p_{H_2}^{2.5}} \left(p_{CH_4} p_{H_2O} - \frac{p_{H_2}^3 p_{CO}}{K_1} \right) / DEN^2 \tag{4}$$

$$r_2 = \frac{k_2}{p_{H_2}} \left(p_{CO} p_{H_2O} - \frac{p_{H_2} p_{CO_2}}{K_2} \right) / DEN^2 \tag{5}$$

$$r_3 = \frac{k_3}{p_{H_2}^{3.5}} \left(p_{CH_4} p_{H_2O}^2 - \frac{p_{H_2}^4 p_{CO_2}}{K_3} \right) / DEN^2 \tag{6}$$

$$k_i = A_i / e^{(E_i/RT)}, \ (i = 1, 2, 3) \tag{7}$$

where $DEN = 1 + K_{CO} p_{CO} + K_{H_2} p_{H_2} + K_{CH_4} p_{CH_4} + K_{H_2O} p_{H_2O} / p_{H_2}$. The pre-exponential factors A_i and activation energies E_i are shown in Table 1.

2. SMR Reactor Structure

A 30 Nm³/h H_2 production system was developed for a pilot H_2/HCNG fueling station as shown in Fig. 1(a) [28]. A 3D CFD model is provided in Fig. 1(b) to elucidate the internal structure of the reactor. The reactor comprised eight duplex reaction tubes and one metal fiber burner in the center of a cylindrical furnace with a diameter of 930 mm and a length of 1,400 mm. The total height, including pipes, insulation, and reformer holders, was 2,200 mm as shown in Fig. 1(c). Ni-based reaction catalysts were filled between inner and outer tubes of 1 in and 3 in diameters, respectively. As shown in Fig. 1(d), feed gas, a mixture of natural gas and steam, enters from the bottom of the catalysts layer and reacts by moving approximately 1,200 mm upward. Then, the reacted product (i.e., reformate) leaves the reactor through the inside of the inner tube. The burner was located at the center of the furnace topside. Flame and heat were generated in the side area of the cylindrical burner. After heat transfer for the endothermic reaction, flue gas is discharged through a 6.6 mm clearance gap passing through the external surface of the reaction tube.

3. Operational Data

The experiment was conducted for 8 h after stabilization. A total of 1,400 samples of temperature, pressure, and flow rate were measured, as shown in Fig. 2. The temperatures of the feed gas, reformate gas, flue gas, reaction tube, and furnace are shown in Fig. 2(a). To precisely measure the reaction tube temperature during an endothermic reaction, nine thermocouples were placed at different points along with the longitudinal positions of the reaction tube. The pressure of the feed and product flow streams of the SMR reactor

(a)　　　　　　　　　　　　　　　　　　　(b)
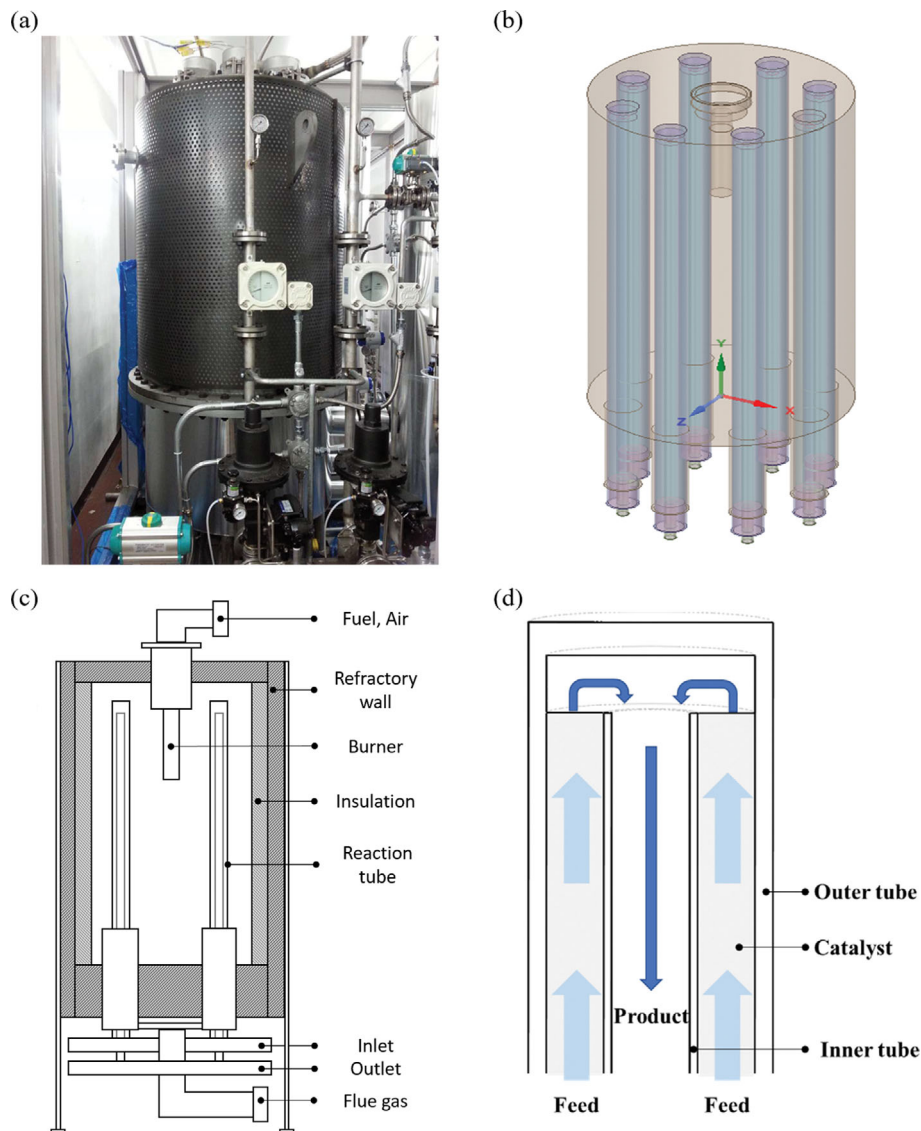
(c)　　　　　　　　　　　　　　　　　　　(d)

Fig. 1. Schematic of SMR reactor: (a) actual SMR reactor used in the experiment, (b) 3D reactor model, (c) side view of SMR reactor, and (d) feed and product flow passing through the catalyst layer between the outer and inner tubes.

was measured to evaluate the pressure drop through the catalysts layer during the chemical reactions as shown in Fig. 2(b). The flow rates for CH_4 and steam as feed materials for the reaction at the initial part of the catalyst layers and fuel with primary and secondary air for combustion at the top side of the furnace were measured as shown in Fig. 2(c).

DEVELOPMENT OF 3D CFD MODEL

A 3D SMR reactor model was developed using CFD simulation software, ANSYS Fluent 2021R1 (ANSYS Inc., USA). As the reactor is a cylindrical symmetric geometry consisting of eight tubes, CFD simulation was performed using only half of a tube (i.e., 1/16 scale) to reduce the computation time.

1. Numerical Setup

The developed model includes standard k-ε turbulence, discrete ordinate (DO) radiation, and species transport models. The opera-

tion of the SMR reactor is assumed to be a steady state as it is governed by the equilibrium state that determines the final product composition. Under the assumption of the steady-state incompressible ideal gas phase, a continuity equation without a second phase or any user-defined sources and a momentum equation with external body force for porous media were adopted as follows.

Continuity equation:
$$\nabla \cdot (\rho \vec{u}) = 0 \tag{8}$$

Momentum equation:
$$\nabla \cdot (\rho \vec{u} \vec{u}) = -\nabla P + \nabla \cdot (\bar{\tau}) + \rho \vec{g} + \vec{F} \tag{9}$$

where the stress tensor is defined in Eq. (10), and the momentum source term for single homogeneous porous media is defined in Eq. (11):

$$\bar{\tau} = \mu \left[(\nabla \vec{u} + \nabla \vec{u}^T) - \frac{2}{3} \nabla \cdot \vec{u} I \right] \tag{10}$$
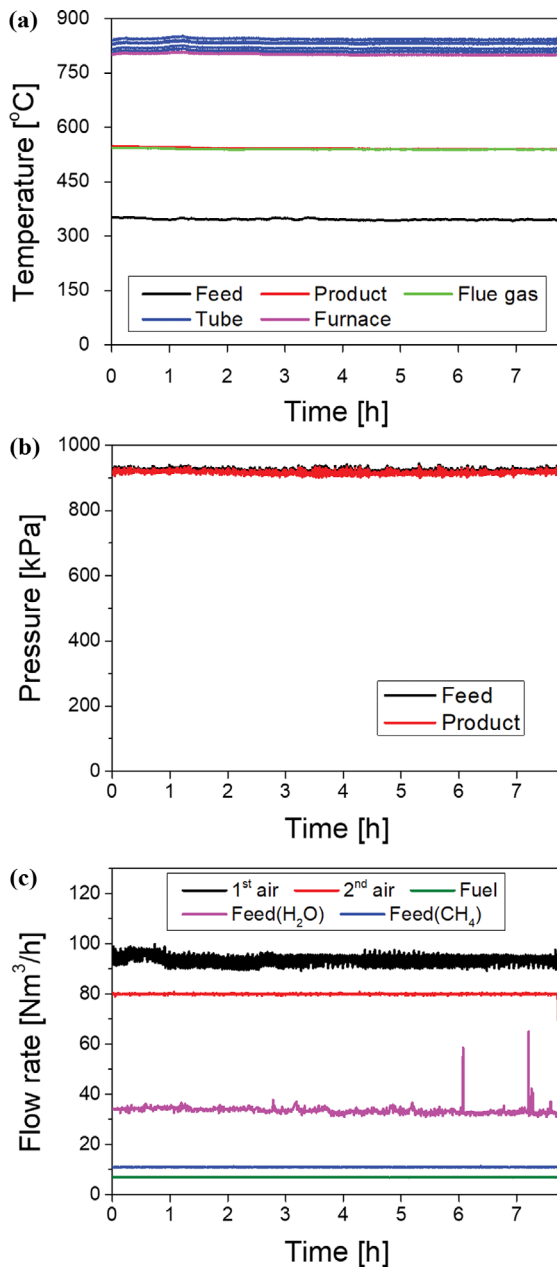
Fig. 2. Measured experimental data of operating conditions: (a) Temperatures of feed, product, flue gas, walls of reaction tubes, and furnace, (b) pressures of feed and product streams, and (c) flow rates of 1st and 2nd air, CH_4 and H_2O feeds, and fuel for combustion.

$$\vec{F} = -\left(\frac{\mu}{\alpha}\vec{u} + C_2\rho\frac{1}{2}|\vec{u}|\vec{u}\right) \quad (11)$$

The permeabilities for the viscous loss term and inertial loss coefficient for the inertial loss term for a packed bed are defined as Eqs. (12) and (13), respectively:

$$\alpha = \frac{D_P^2}{150\mu} \frac{\gamma^3}{(1-\gamma)} \quad (12)$$

$$C_2 = \frac{3.5(1-\gamma)}{D_P} \frac{1}{\gamma^3} \quad (13)$$

The standard k-ε turbulence model is widely used because it is robust and reasonably accurate for a variety of applications, such as pipe and flat plate flows. It is available for a wide range of Reynolds numbers from 150 to 3×10^3, making it applicable from laminar boundary layer flows to the separation point, turbulent wake, and fully turbulent flows. The standard k-ε turbulence equations are

$$\frac{\partial}{\partial x_i}(\rho k u_i) = \frac{\partial}{\partial x_j}\left[\left(\mu + \frac{\mu_t}{\sigma_k}\right)\frac{\partial k}{\partial x_j}\right] + G_k + G_b - \rho\varepsilon \quad (14)$$

$$\frac{\partial}{\partial x_i}(\rho\varepsilon u_i) = \frac{\partial}{\partial x_j}\left[\left(\mu + \frac{\mu_t}{\sigma_\varepsilon}\right)\frac{\partial\varepsilon}{\partial x_j}\right] + G_{1\varepsilon}\frac{\varepsilon}{k}(G_k + G_{3\varepsilon}G_b) - C_{2\varepsilon}\rho\frac{\varepsilon^2}{k} \quad (15)$$

where

$$G_k = \mu_t S^2 \quad (16)$$

$$S \equiv \sqrt{2S_{ij}S_{ij}} \quad (17)$$

$$S_{ij} = \frac{1}{2}\left(\frac{\partial u_j}{\partial x_i} + \frac{\partial u_i}{\partial x_j}\right) \quad (18)$$

$$G_b = -\beta g_i \frac{\mu_t}{Pr_t}\frac{\partial\rho}{\partial x_i} \quad (19)$$

$$\beta = \frac{1}{\rho}\left(\frac{\partial\rho}{\partial T}\right)_p \quad (20)$$

$$\mu_t = \rho C_\mu \frac{k^2}{\varepsilon} \quad (21)$$

The generation of turbulence kinetic energy, defined using the Boussinesq hypothesis for an eddy viscosity model with an alignment between the Reynolds stress and mean strain tensors, is caused by the gradient of the mean velocity G_k (Eq. (16)) and the buoyancy G_b (Eq. (19)) for ideal gases. Eq. (17) is the modulus of the mean rate-of-stress tensor S, Eq. (20) is the coefficient of thermal expansion β, and Eq. (21) is the dissipation rate μ_t. The constants and turbulent Prandtl number for k and ε are $C_{1\varepsilon}$=1.44, $C_{2\varepsilon}$=1.92, C_μ=0.09, σ_k=1.0, σ_ε=1.3.

In the energy equation for conductive and convective heat transfer as shown in Eq. (22), three terms on the right-hand side of the equation represent energy transfer caused by conduction, species diffusion, and viscous dissipation, respectively,

$$\nabla\cdot\left(\rho v\left(h + \frac{v^2}{2}\right)\right) = \nabla\cdot(k_{eff}\nabla T - \Sigma_j h_j \vec{J}_j + \bar{\bar{\tau}}_{eff}\cdot\vec{v}) + S_h \quad (22)$$

where

$$h = c_p T + \frac{P}{\rho} \quad (23)$$

$$k_{eff} = k + \frac{c_p\mu_t}{Pr_t} \quad (24)$$

The source of energy, S_h, includes volumetric heat sources, radiative heat sources, and heat generation from chemical reactions. Enthalpy for incompressible ideal gases, h, is defined as Eq. (23), and the effective thermal conductivity, k_{eff}, is defined as a combination of thermal conductivity and turbulent thermal conductivity as in Eq. (24).
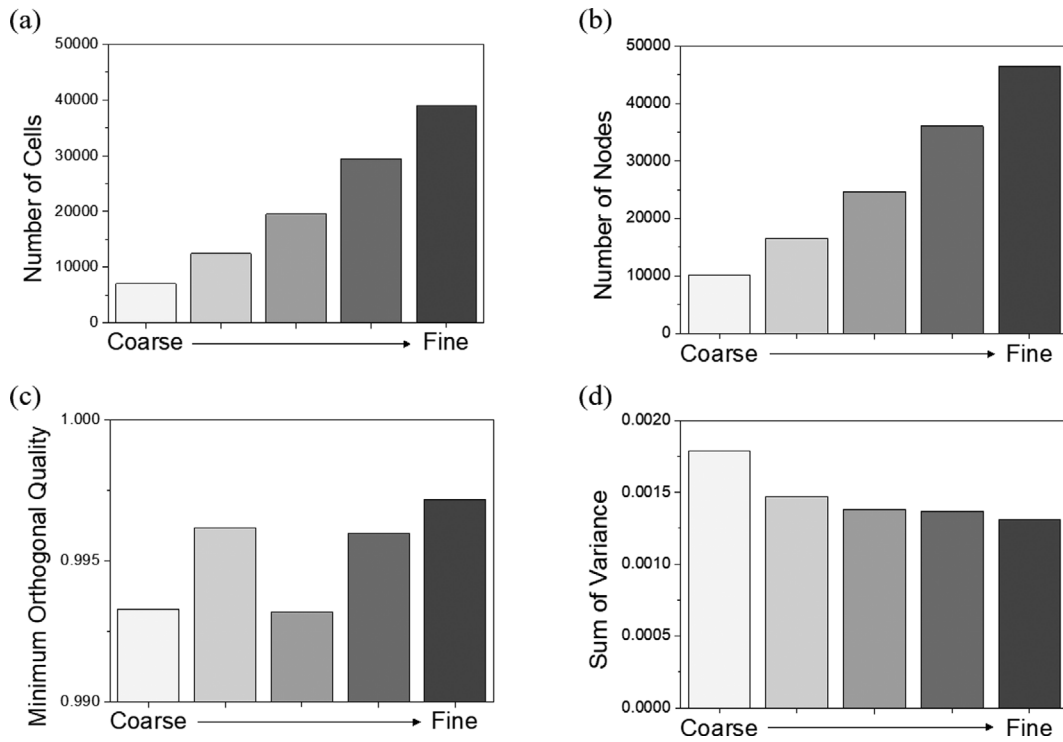
(a)

(b)

(c)

(d)

Fig. 3. Change in properties with five distinct mesh densities: (a) Number of cells, (b) number of nodes, (c) minimum orthogonal quality, and (d) sum of the variance of compositions between theoretical values and CFD model.

In the solid phase, the energy transport equation is defined as

$$\nabla \cdot (v\rho h) = \nabla \cdot (k\nabla T) + S_h \tag{25}$$

$$h = \int_{298.15\,K}^{T} C_{p,j} dT \tag{26}$$

where the enthalpy (Eq. (26)) includes changes in the specific heat for the pressure-based solver.

Radiative heat transfer is dominant and accounts for approximately 95% of the SMR reactor, which is under high-temperature conditions [29]. The DO radiation model can adapt to the entire range of optical thickness with moderate computational cost and parallel processing. It is also possible to apply complex geometry, porous media, symmetry boundary condition, and localized heat source as in this study. The DO radiative transfer equation (Eq. (27)) describes the steady-state conservation of radiant energy of a single ray traveling in direction s from position r.

$$\nabla \cdot (I(\vec{r}, \vec{s})\vec{s}) = an^2 \frac{\sigma T^4}{\pi} + \frac{\sigma_s}{4\pi} \int_0^{4\pi} I(\vec{r}, \vec{s}') \Phi(\vec{s}, \vec{s}') d\Omega' - (a + \sigma_s) I(\vec{r}, \vec{s}) \tag{27}$$

Three terms on the right-hand side of Eq. (27) represent the gain of intensity caused by blackbody emission, the gain of intensity caused by in-scattering effects for the entire range of solid angles from 0 to 4π steradian, and the loss of intensity caused by absorption and out-scattering effects, respectively [30].

The species transport equation (Eq. (28)) contains mass diffusion, which arises because of the gradient of temperature and composition, J_i, defined in Eq. (29), and the net rate of production by chemical reaction, R_i:
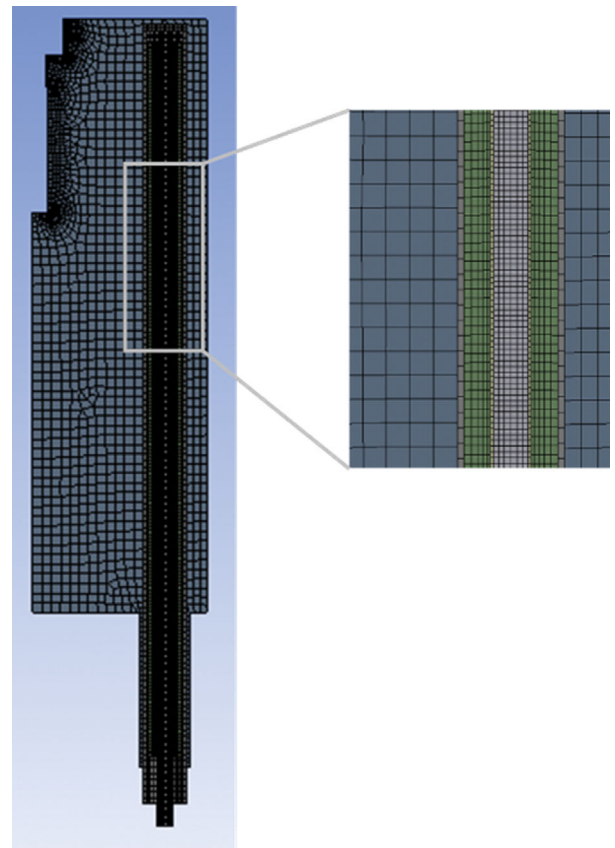
Fig. 4. Computational domain and structured hexahedral mesh of 1/16th symmetrically scaled SMR reactor.

Table 2. Mesh quality of the reformer

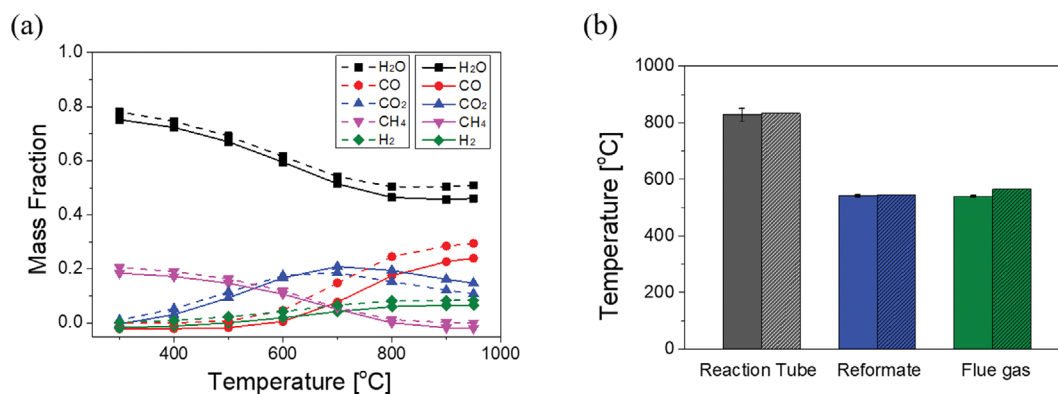|	Recommended range (ideal values) (31)	Average value of the proposed reformer
Orthogonal quality	0.167-1.000 (1.000)	0.8406
Skewness	0.000-0.850 (0.000)	0.2482
Aspect Ratio	1.000-100.0 (1.000)	5.7431

Fig. 5. (a) Gas composition calculated by HSC Chemistry (solid line) and CFD kinetic model (dashed line), and (b) temperature of the reactor tube, reformate, and flue gas measured in the experiment (left colored bar) and calculated via CFD model (right dashed colored bar).

$$\nabla \cdot (\rho \vec{u} Y_i) = -\nabla \cdot \vec{J}_i + R_i \tag{28}$$

$$\vec{J}_i = -\left(\rho D_{m,i} + \frac{\mu_t}{Sc_t}\right)\nabla Y_i - D_{T,i}\frac{\Delta T}{T} \tag{29}$$

2. Mesh Generation

Because mesh structure and quality affect the accuracy of the CFD results and calculation time, the reformer mesh must have a reasonable agreement with a recommended quality range. Therefore, the mesh structure and dependency of the catalyst layer, which comprise an important chemical reaction, were evaluated as shown in Fig. 3. Comparing five different cases from coarse to fine meshes, the number of cells and nodes of the catalyst layer increased linearly, as shown in Figs. 3(a) and 3(b), respectively. The orthogonal quality of the third case was relatively low, as shown in Fig. 3(c). The differences in the composition variance between the theoretical calculation and CFD results are insignificant for the second to fifth cases, as shown in Fig. 3(d). Consequently, the mesh of the fourth case was chosen as an optimal structure for the catalyst layer.

Furthermore, a 1/16th symmetry domain of hexahedral meshes was selected to reduce the computation time of CFD simulation, as shown in Fig. 4.

The average values of the orthogonal quality, skewness, and aspect ratio of the mesh structures of the reactor were calculated as 0.8406, 0.2482, and 5.7431, respectively, as shown in Table 2. These average values are within the ranges recommended in [31] and reasonably close to the ideal values of 1.000, 0.000, and 1.000 for orthogonal quality, skewness, and aspect ratio, respectively.

3. Model Validation

The proposed CFD model of an equilibrium limited SMR process was compared with the theoretical equilibrium state calculated using HSC Chemistry 9 software (Metso Outotec, Finland) to evaluate the feasibility of the CFD reaction kinetic model. As

shown in Fig. 5(a), the CFD model and theoretical calculations were compared in terms of the mass fraction. The mass fractions of the five gases in the CFD model for the temperature range from 300 °C to 1,000 °C are consistent with the theoretical equilibrium compositions. The general SMR reaction is thermodynamically advantageous at high temperatures, but it is also operated at low temperatures for safety reasons because small-scale reformers are more likely to be operated in the proximity of the end-user. Therefore, a wide range of temperatures from 300 °C to 1,000 °C is considered to expand the applicability of the developed model. The mean absolute errors for H_2O, CO, CO_2, CH_4, and H_2 were 0.011, 0.024, 0.031, 0.0054, and 0.0017, respectively.

The temperature values of the upper side of the reaction tube and steam flows of the reformate and flue gas were compared with experimental data, as shown in Fig. 5(b). The absolute error of the temperature of the upper side of the reaction tube, reformate flow, and flue gas was 5.93, 3.44, and 25.89, respectively. The temperature error of the flue gas was relatively large owing to the heat loss, because the flue gas exhaust pipe is located at the outermost side and remains in contact with the atmosphere during the experiment.

RESULTS AND DISCUSSION

1. Comparison of Reactor Designs

The reactor performance was evaluated according to changes in reactor structure, size, and the amount of packed catalyst to propose criteria for design improvement. As shown in Fig. 6(a), the reference case is herein referred to as case 1A. Cases 2-4A indicate a reduction of 0.8, 0.6, 0.4 times from the height of the reformer of case 1A, respectively, as shown in Fig. 6(b)-6(d); cases 5A and 6A indicate a reduction of 0.8 and 0.6, respectively, of the distance between the reformer center and reaction pipe center, as shown in
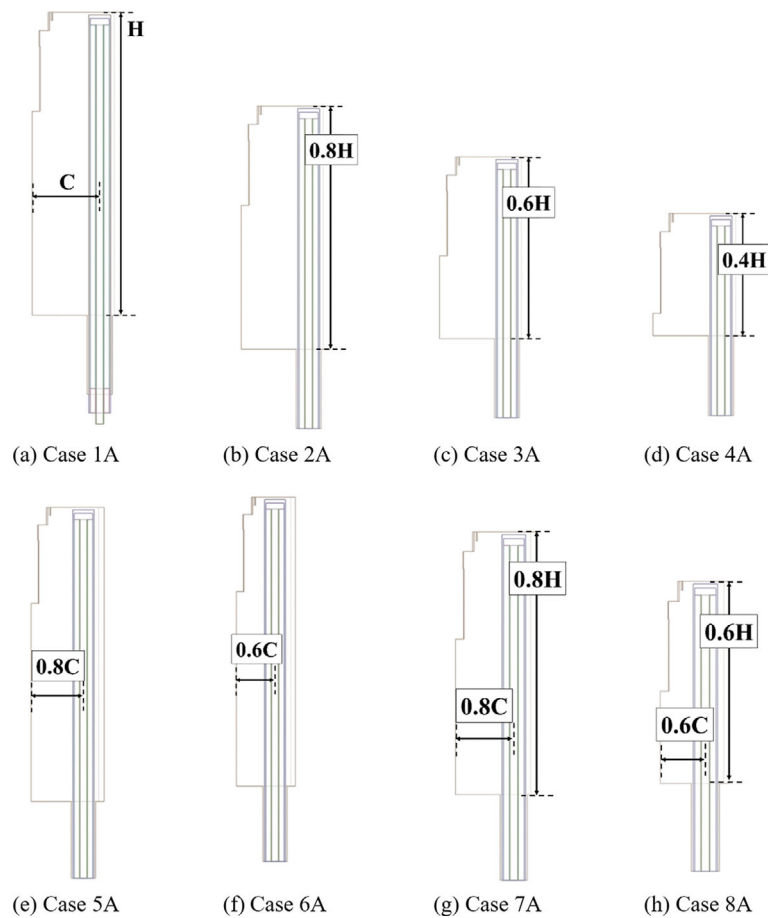
Fig. 6. Eight different reactor dimensions for case study: (a) Case 1A as reference model, (b) case 2A with 80% height, (c) case 3A with 60% height, (d) case 4A with 40% height, (e) case 5A with 80% center distance, (f) case 6A with 60% center distance, (g) case 7A with 80% height and 80% center distance, and (h) case 8A with 60% height and 60% center distance.
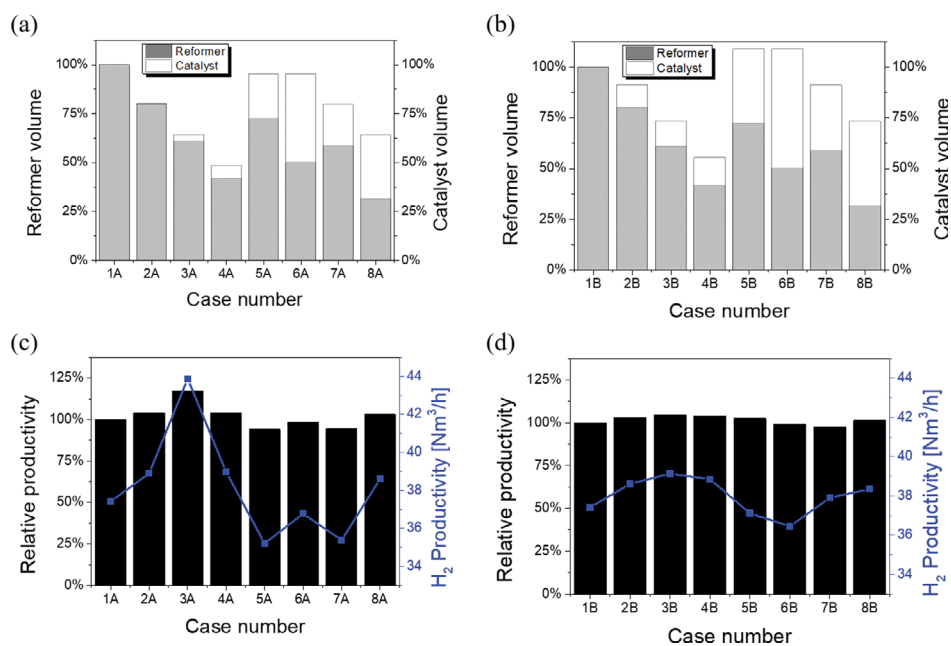

Fig. 7. Effect of SMR reactor structure on reformer and catalyst volumes and H_2 productivity: (a) Reformer and catalyst volumes in cases 1-8A, (b) reformer and catalyst volumes in cases 1-8B with reduced NPS, (c) relative and absolute productivity of H_2 in cases 1-8A, and (d) relative and absolute productivity of H_2 in cases 1-8B with reduced NPS.

Table 3. Calculation results of CFD simulation for 16 cases

	Reformer volume (%)	Catalyst volume (%)	Reformer volume (m³)	Catalyst volume (m³)	Relative productivity (%)	H₂ productivity (Nm³/h)
Case 1A	100.00	100.00	0.534	0.049	100.00	37.423
Case 2A	80.01	79.71	0.428	0.039	103.94	38.899
Case 3A	60.87	64.08	0.325	0.031	117.24	43.877
Case 4A	41.77	48.45	0.223	0.024	103.92	38.889
Case 5A	72.35	95.35	0.387	0.047	94.11	35.217
Case 6A	49.98	95.35	0.271	0.047	98.27	36.775
Case 7A	58.59	79.71	0.313	0.039	94.57	35.217
Case 8A	31.41	64.08	0.168	0.031	103.17	38.609
Case 1B	100.00	100.00	0.534	0.049	100.00	37.423
Case 2B	80.01	91.01	0.428	0.045	103.20	38.621
Case 3B	60.88	73.16	0.325	0.036	104.59	39.142
Case 4B	41.77	55.32	0.223	0.027	103.83	38.856
Case 5B	72.38	108.86	0.387	0.053	99.20	37.125
Case 6B	50.00	108.86	0.271	0.053	97.41	36.454
Case 7B	58.61	91.01	0.313	0.045	101.31	37.914
Case 8B	31.42	73.16	0.168	0.036	102.48	38.352

Fig. 6(e) and 6(f); and cases 7A and 8A show a reduction of 0.8 and 0.6, respectively, in both height and center distance, as shown in Fig. 6(g) and 6(h). Cases 1-8B have a smaller inner-tube size in terms of normal pipe size (NPS) (1/2 in) without changing the size of the reformer in cases 1-8A, respectively, to increase the packed catalyst volume. Therefore, the case study included a total of 16 different reactor structures.

2. Productivity Depending on SMR Reactor Structure

The reactor volume, catalyst volume, and performance of the reference case 1A were set to 100%, and each case was compared to the reference model value. As shown in Fig. 7(a), cases 2-4A have smaller reformer and catalyst volumes than cases 1A. Cases 5A and 6A have the same catalyst volume but reduced reformer volume. Cases 7A and 8A have reduced catalyst and reformer volumes. Fig. 7(b) shows the reformer and catalyst volume with reduced inner tube NPS. The volume of the catalyst for cases 2-8B increases while maintaining the volume of the reformer with the reduced NPS of the inner tube, compared to the volume for 2-8A.

As shown in Fig. 7(c), H₂ production increased by 17.24% for case 3A when the reformer volume was 60.87% of the reference model by scaling down the height. When the reformer volume decreased to 72.35% (case 5A) and 49.98% (case 6A) of the reference model by scaling down the center distance, productivity decreased. The main difference is the packed catalyst volume. The reference model had an excessive catalyst volume for its production capacity. Case 4A showed lower productivity than case 3A. Fig. 7(d) presents a similar trend as Fig. 7(c), whereas it has a lower difference in productivity when compared to the reference model. It shows that excessive catalysts can reduce productivity. Hence, an appropriate packed catalyst volume is required. Case 3A was selected as the most optimal reactor structure based on H₂ productivity.

It was then observed that the production performance decreased because of a reverse reaction that occurred from the end of the reforming reaction when the catalyst charge amount was excessive

compared with the production capacity. Even when the amount of catalyst was excessively decreased, its performance deteriorated. Thus, the reformer should be designed for the reforming reaction to occur evenly throughout the entire catalyst layer. The detailed
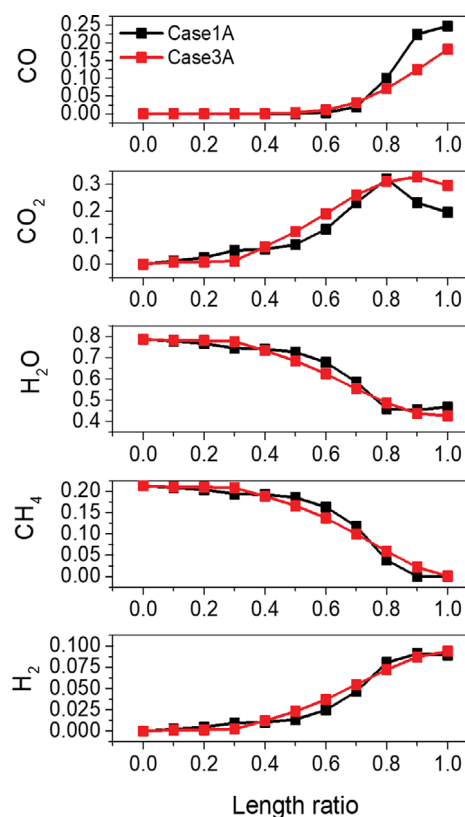

Fig. 8. Mass fractions of the five gases in optimal case 3A (red) and reference case 1A (black) depending on the position of the reforming catalyst layer.

results of H_2 productivity and reformer and catalyst volumes are presented in Table 3.

3. Gas Composition and Reaction Rate

The optimal reactor structure of case 3A was analyzed in detail to determine the factors causing the observed differences. The starting point of the feed gas was set to 0.0 and the top of the catalyst (i.e., the point at which the reaction was finished) was set to 1.0. The mass fraction of each gas composition along the reforming catalyst position was analyzed and compared, as shown in Fig. 8. In case 3A, the mass fraction of all components gradually increased or decreased, whereas the reference model of case 1A had

the singularity at a length ratio of 0.8. From this point, CO_2 started to decrease sharply, and H_2O and CO increased.

From the analysis of contour results of kinetic rate of reactions, as shown in Fig. 9, the area and distribution of each reaction were investigated. In the case of the reference model (Fig. 9(a)-(d)), the reactions did not utilize the catalyst layer evenly and concentrated only in some areas. Moreover, the reverse reaction of reaction (2) was prominent at the top of the catalyst layer, compared with case 3A. This is related to the increase in CO_2 at the length ratio of 0.8, as shown in Fig. 7. Thus, as H_2 production was concentrated in a part of the catalyst layer, a reverse reaction occurred in which the
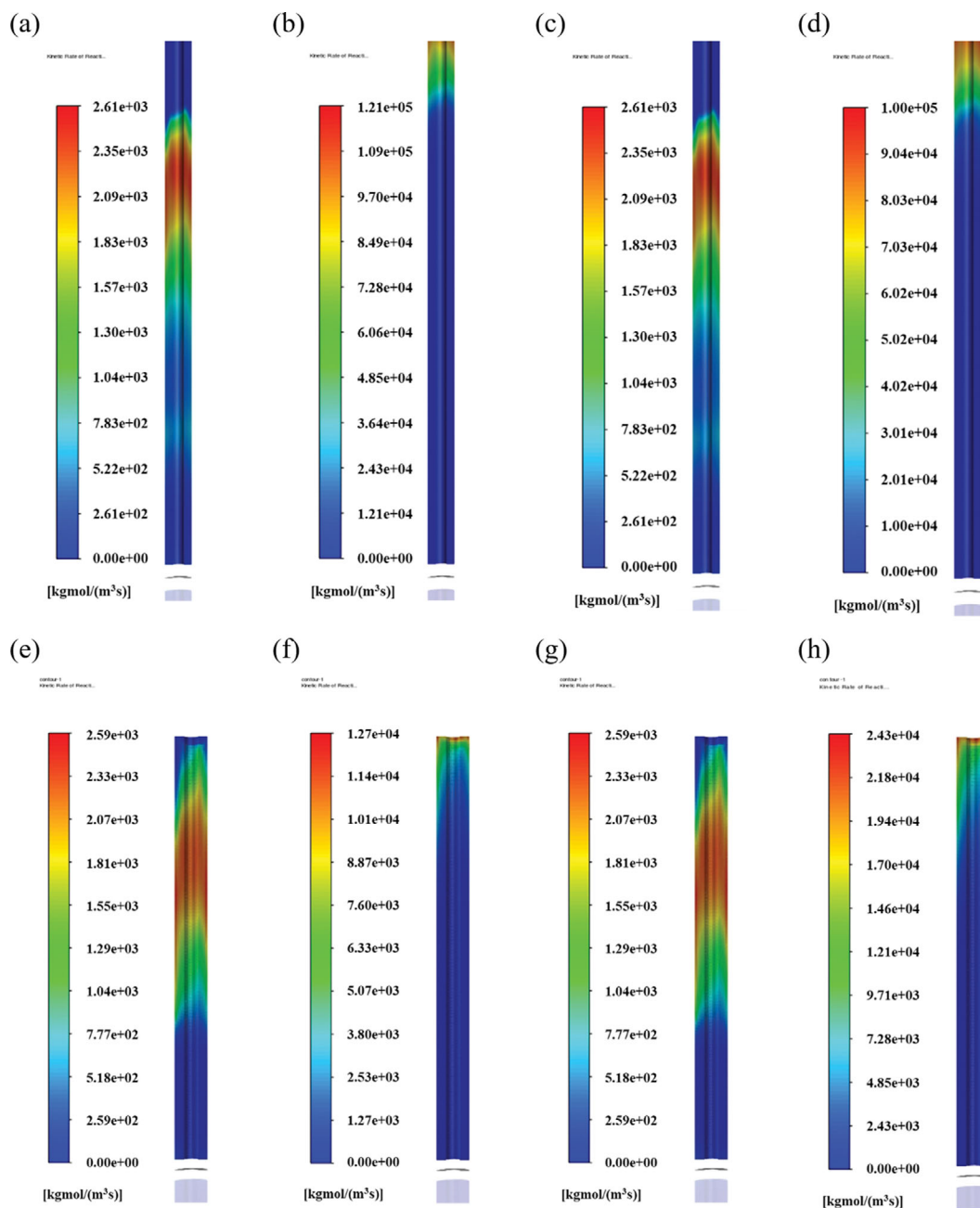

Fig. 9. Rate of reaction along the catalyst layer: (a) reaction (1), (b) reaction (2), (c) reaction (3), and (d) reverse reaction of reaction (2) of reference case 1A; (e) reaction (1), (f) reaction (2), (g) reaction (3), and (h) reverse reaction of reaction (2) of optimal case 3A.
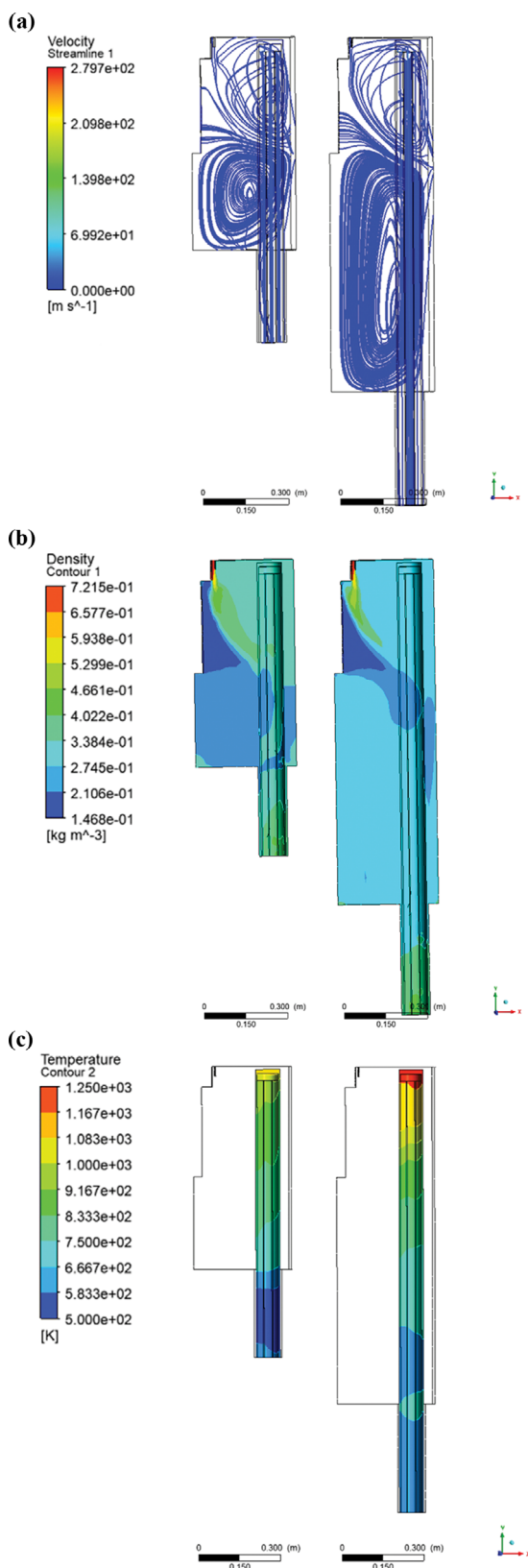
(a)

(b)

(c)

Fig. 10. SMR reactor characteristics in optimal case 3A and reference case 1A: (a) Streamlines in cases 3A (left) and 1A (right), (b) density distribution in cases 3A (left) and 1A (right), and (c) temperature distribution of outer tube in cases 3A (left) and 1A (right).

produced H_2 and CO_2 returned to CO and H_2O in the remaining area. For case 3A (Fig. 9(e)-(h)), which showed improved productivity compared with the reference case, reactions (1) and (3) were distributed in a relatively spacious area of the catalyst layer, whereas reaction (2) and the reverse reaction of reaction (2) occurred at the end of the catalyst layer. The reverse reaction of reaction (2) is more dominant than the forward reaction of reaction (2) at high temperature because the WGS reaction is exothermic. Therefore, the reverse reaction of reaction (2) was additionally investigated as shown in Fig. 9(d) and (h).

4. SMR Reactor Characteristics

Fig. 10(a) shows streamlines for case 3A and the reference model case 1A. The flow occurs in the horizontal direction from the metal fiber burner. In the vertical direction, secondary air enters from the top of the reformer to prevent the concentration of heat and promote heat flow. Flue gas burns out of the exhaust in the lower part. In the case of the reference model, the distance from the burner to the flue gas outlet is long, hence the flow is elongated; case 3A shows a slightly more compressed flow.

Fig. 10(b) shows the density distribution with the same scale to compare the two cases. In case 3A, the density is focused on the upper part of the reaction tube, which undergoes chemical reactions, whereas the reference case has a lower density across the broad area. In particular, the reference case has a lower density area where reforming reactions mainly occur. The high density of fluid means sufficient flow flux with high Reynolds numbers; hence, it is important to consider the heat and mass flux.

Fig. 10(c) shows the temperature distribution of the outer reaction tube. The temperature of the reaction tube is considered a crucial factor because it directly affects the physical stability and lifespan of the reactor. Additionally, the tube thickness is determined according to its maximum temperature. Therefore, it is highly related to manufacturing costs. In case 3A, the reforming reaction takes place across nearly the entire reaction tube, as shown in Fig. 9. Accordingly, the temperature of the external reaction tube does not increase significantly, and no hot spot occurs, caused by the steam reforming reactions, which are strong endothermic reactions. On the other hand, in the reference model, the steam reforming reactions are concentrated in the central part of the reaction tube, and most of the reforming reactions are completed before reaching the upper part. Therefore, a hot spot has occurred at the top of the reaction tube.

When the reaction was concentrated only in a part of the reaction tube, heat accumulated in areas where the reaction did not occur, resulting in hot spots. As the distance between the reactor and the center of the reaction tube was reduced, the maximum temperature delivered to the reaction tube increased, increasing H_2 production. However, this factor did not have a greater effect than the change in the amount of catalyst created by adjusting its height.

CONCLUSIONS

A small-scale steam reforming reactor for an H_2 charging station or fuel cell requires a fixed installation area and production capacity. Thus, the reactor size should be compact while the production efficiency is maintained. In this study, experiments were

conducted with an SMR reactor installed in a pilot H$_2$/HCNG refueling station and the experimental results were employed to develop a corresponding 3D CFD model that simultaneously predicts the composition and temperature. The proposed model is a prediction model with high practicality that can be used in real industry. H$_2$ production efficiency was examined depending on the change in the reactor size, i.e., the height of the reformer and the reaction tube, the distance between the center of the reformer and the center of the reaction tube, and the case where both were reduced simultaneously. Additionally, the amount of catalyst charged was changed by reducing the normal pipe size of the inner tube, keeping the size change of the reactor the same. Among a total of 16 reactor structures, the reformer of case 3A with a height of 1.32 m was found to be optimal in terms of H$_2$ productivity. The proposed optimal configuration of a compact steam reformer with stable productivity can be used for on-site H$_2$ production.

NOMENCLATURE

a : radiation absorption coefficient [1/m]
A_i : pre-exponential factor of rate coefficient k_i
C_p : heat capacity at constant pressure [J/kg·K]
D_p : diameter of catalyst particle [m]
D_m : mass diffusion coefficient [m^2/s]
D_T : thermal diffusion coefficient [m^2/s]
E_i : activation energy [kJ/mol]
g : gravitational acceleration [m/s^2]
g_i : gravitational vector in the ith direction
h : enthalpy [J/kg]
h^0 : enthalpy of formation [J/kg]
I : radiation intensity [W/m^2·sr]
J : diffusion flux [kg/m^2·s]
k : turbulent kinetic energy [m^2/s^2]
k_1, k_3 : rate coefficient [kmol bar$^{1/2}$/kg·h]
k_2 : rate coefficient [kmol/kg·h·bar]
$K_{CH_4}, K_{CO}, K_{H_2}$: adsorption constant [bar^{-1}]
K_{H_2O} : dissociative adsorption constant
M : molecular weight [kg/kmol]
n : refractive index
P_j : partial pressure of component j [bar]
Pr_t : turbulent Prandtl number
R : gas constant [kJ/kmol·K]
R_j : volumetric rate of creation of species j
r : refractive index of the medium
r_1, r_2, r_3 : rate of reaction rate [kmol/kg·h]
Sc_t : turbulent Schmidt number
S_{ij} : mean rate of the strain tensor [1/s]
T : temperature [K]
u : velocity [m/s]
v : velocity [m/s]
V_s : superficial velocity [m/s]
x : length [m]
Y : mass fraction of component

Greek Symbols

α : permeability [m^2]

β : coefficient of thermal expansion [1/K]
ε : turbulent dissipation rate [m^2/s^3]
γ : porosity
μ : dynamic viscosity [Pa·s]
μ_t : turbulent viscosity [kg/m·s]
Ω' : solid angle [rad]
ρ : mass density of a gas mixture [g/cm^3]
σ : Stefan-Boltzmann constant [5.672×10^{-8} W/m^2·K^4]
$\sigma_k, \sigma_\varepsilon$: turbulent Prandtl number
σ_s : scattering coefficient [1/m]
$\bar{\tau}$: stress tensor [Pa]
τ : shear stress [Pa]

REFERENCES

1. E. E. R. ENERGY (Hydrogen Production: Natural Gas Reforming).
2. A. Demirbas, *Energy Sources B: Econ. Plan. Policy*, **12**, 172 (2017).
3. R. B. Gupta, *Hydrogen fuel - production, transport and storage*, CRC Press (2009).
4. P. Nikolaidis and A. Poullikkas, *Renew. Sust. Energ. Rev.*, **67**, 597 (2017).
5. A. P. Simpson and A. E. Lutz, *Int. J. Hydrogen Energy*, **32**, 4811 (2007).
6. N. Hajjaji, M.-N. Pons, A. Houas and V. Renaudin, *Energy Policy*, **42**, 392 (2012).
7. P. Li, L. Chen, S. Xia and L. Zhang, *Int. J. Chem. React.*, **17**, 20180191 (2019).
8. M. Taji, M. Farsi and P. Keshavarz, *Int. J. Hydrogen Energy*, **43**, 13110 (2018).
9. M. S. Nobandegani, M. R. S. Birjandi, T. Darbandi, M. M. Khalilipour, F. Shahraki and D. Mohebbi-Kalhori, *J. Nat. Gas Sci. Eng.*, **36**, 540 (2016).
10. C. M. Kallegoda, CH 4034 Comprehensive Design Project II Interim Report 1 Primary Reformer Design Production of Ammonia from Naphtha, D. P. G. Rathnasiri (2017).
11. A. Tran, A. Aguirre, M. Crose, H. Durand and P. D. Christofides, *Comput. Chem. Eng.*, **104**, 185 (2017).
12. A. Kumar, T. F. Edgar and M. Baldea, *Comput. Chem. Eng.*, **107**, 271 (2017).
13. A. Kumar, M. Baldea and T. F. Edgar, *Comput. Chem. Eng.*, **105**, 224 (2017).
14. A. Kumar, M. Baldea and T. F. Edgar, *Control Eng. Pract.*, **54**, 140 (2016).
15. P. Chen, W. Du, M. Zhang, F. Duan and L. Zhang, *Int. J. Hydrogen Energy*, **44**, 15704 (2019).
16. M. M. Aslam Bhutta, N. Hayat, M. H. Bashir, A. R. Khan, K. N. Ahmad and S. Khan, *Appl. Therm. Eng.*, **32**, 1 (2012).
17. M. J. H. Khan, M. A. Hussain, Z. Mansourpour, N. Mostoufi, N. M. Ghasem and E. C. Abdullah, *J. Ind. Eng. Chem.*, **20**, 3919 (2014).
18. K. Uebel, P. Rößger, U. Prüfert, A. Richter and B. Meyer, *Fuel Process. Technol.*, **149**, 290 (2016).
19. Z. Bao, F. Yang, Z. Wu, S. Nyallang Nyamsi and Z. Zhang, *Energy Convers. Manag.*, **65**, 322 (2013).
20. J. Ding, X. Wang, X. F. Zhou, N. Q. Ren and W. Q. Guo, *Bioresour. Technol.*, **101**, 7016 (2010).

21. J. L. Ansoni and P. Seleghim, *Adv. Eng. Softw.*, **91**, 23 (2016).

22. S. Park, J. Na, M. Kim and J. M. Lee, *Comput. Chem. Eng.*, **119**, 25 (2018).

23. G. Shin, J. Yun and S. Yu, *Int. J. Hydrogen Energy*, **42**, 14697 (2017).

24. S. K. Hong, S. K. Dong, J. O. Han, J. S. Lee and Y. C. Lee, *Energy*, **61**, 410 (2013).

25. D. D. Nguyen, S. I. Ngo, Y. I. Lim, W. Kim, U. D. Lee, D. Seo and W. L. Yoon, *Int. J. Hydrogen Energy*, **44**, 1973 (2019).

26. S. I. Ngo, Y.-I. Lim, W. Kim, D. J. Seo and W. L. Yoon, *Appl. Energy*, **236**, 340 (2019).

27. J. Xu and G. F. Froment, *AICHE Symp. Ser.*, **35**, 88 (1989).

28. J. Han, A Development of Engine and Fuelling Station for HCNG fueled City Bus (2016).

29. Z. Yu, E. Cao, Y. Wang, Z. Zhou and Z. Dai, *Fuel Process. Technol.*, **87**, 695 (2006).

30. P. C. J. Hoi, Validation of discrete ordinate radiation model for application in UV air disinfection modeling (2014).

31. A. Tran, A. Aguirre, H. Durand, M. Crose and P. D. Christofides, *Chem. Eng. Sci.*, **171**, 576 (2017).